Accepted Manuscript

X-ray speckle reduction using a high-speed piezoelectric deformable mirror system

Shuai Yan[1], Hui Jiang[1,2,*], Zhisen Jiang[1], Dongxu Liang[1], Jianan Xie[1,3], Hai Zhu[4,*], Guoyang Shu[4], Ningyu Ben[4] and Aiguo Li[1,2]

[1] *Shanghai Synchrotron Radiation Facility, Shanghai Advanced Research Institute, Chinese Academy of Sciences, 239 Zhangheng Road, Pudong District, Shanghai, 201204, China;*

[2] *Shanghai Institute of Applied Physics, Chinese Academy of Sciences, 2019 Jialuo Road, Jiading District, Shanghai, 201800, China;*

[3] *Nankai University, 38 Tongyan Road, Jinnan District, Tianjin, 300350, China;*

[4] *Huawei Technologies Co., Ltd, Bantian, Longgang District, Shenzhen, Guangdong Province, 518129, China;*

*Correspondence to: Address of corresp. Emails: jiangh@sari.ac.cn, zhuhai12@huawei.com

Abstract An advanced deformable Kirkpatrick-Baez mirror system was developed, equipped with high-speed piezoelectric actuators, designed to induce beam decoherence and significantly enhance the quality of X-ray imaging by minimizing undesirable speckles in synchrotron radiation or free-electron laser facilities. Each individual mirror is engineered with 36 independent piezoelectric actuators that operate in a randomized manner, orchestrating the mirror surface to oscillate at an high frequency up to 100 kHz.

Through *in-situ* imaging, single-slit diffraction measurement, it has been demonstrated that

10.1017/hpl.2025.7

this high-frequency-vibration mirror system is pivotal in disrupting the coherent nature, thereby diminishing speckle formation.The impact of the K-B mirror system is profound, with the capability to reduce the image contrast to as low as 0.04, signifying a substantial reduction in speckle visibility. Moreover, the coherence of the X-ray beam is significantly lowered from an initial value exceeding 80% to a mere 13%.

Key words: X-ray; Decoherence; Speckle; High-speed deformable mirror

I. INTRODUCTION

In comparison to the third-generation synchrotron radiation light sources, the novel advanced light sources, such as X-ray free electron lasers (XFELs) and diffraction-limited-ring synchrotron radiation facilities, provide significantly enhanced brightness and coherence. For instance, high-gain, high repetition-rate XFELs [1] operating in the self-amplified spontaneous emission (SASE) mode can generate coherent X-ray pulses with gigawatt-level power and femtosecond-level time intervals. These advancements are particularly beneficial for a range of X-ray techniques such as time-resolved imaging [2], ptychography [3], projection holography [4], photon correlation spectroscopy [5], facilitating cutting-edge scientific research. However, there are still some high-resolution imaging applications, especially ultrafast full-field [6] or projection imaging experiments, that need to avoid the presence of coherence when using such ultra-bright beams. The enhanced beam coherence also introduces the speckle phenomenon as background scattering, characterized by granular or noisy patterns resulting from the interference of coherent wavefronts with the surface irregularities of reflective or diffractive optics, beryllium or diamond windows and slit edges. Due to the unavoidable use of optical elements during the beam transmission process and the difficulty in controlling the surface shape of the elements to fully meet Rayleigh

https://doi.org/10.1017/hpl.2025.7 Published online by Cambridge University Press

Criterion, these speckles cannot be avoided. Speckle degrades the signal-to-noise ratio or obscures the weak scattering from sample, thereby diminishing image quality, contrast, and resolution [7]. Additionally, speckle affects the precision of X-ray spectroscopy [8] by altering the intensity distribution across the spectrum, leading to inaccuracies in determining elemental composition, chemical states, and other spectroscopic parameters. Furthermore, the short, extremely intense X-ray pulses produced by XFELs are particularly susceptible to speckle. Fluctuations in the X-ray pulse due to speckle compromise the consistency and reliability of time-resolved studies. Addressing the speckle issue is therefore crucial for the advancement and optimization of X-ray applications in scientific research.

Various strategies have been proposed to spatial decoherence in the visible light spectrum, including the use of moving diffusers [9], polarization adjustments [10], deploying multiple beams with varying angles or wavelengths [11], and employing active deformable mirrors [12,13] as part of optical decoherence schemes. In the realm of visible light projection, deformable mirrors have been instrumental in wavefront control [14,15] and reducing speckle noise [11,12] during imaging processes. These mirrors consist of numerous actuating elements, each capable of independently manipulating the mirror surface to induce the required deformation and correct wavefront aberrations. However, wavefront modulation in the X-ray domain necessitates superior surface control due to the shorter wavelengths involved. Grazing-incidence deformable mirrors were successfully employed in X-ray diffraction-limited focusing systems to correct aberrations to realize wavefront preservation [16,17] or were used directly as a bending actuators to form the desired surface profile of the mirror [18,19]. This kind of mirrors is capable of correcting the mirror's curvature with a high degree of precision, albeit with relatively slow response or closed-loop time at a refresh rate up to 1 kilohertz (kHz), due to the use of actuators

https://doi.org/10.1017/hpl.2025.7 Published online by Cambridge University Press

functioning in bimorph mode. In the X-ray domain, there have been previous studies that attempted to eliminate speckles or background noise in imaging by using moving diffuser [20,21] and altering the tilt angle of the mirror [22]. However, these studies did not address high frequencies, making such devices insufficient for applications involving high-repetition-rate light sources, given that synchrotron radiation beams commonly operate in the megahertz (MHz) frequency range, while XFELs often feature high repetition rates in the hundreds of kilohertz (kHz). Therefore, it is very necessary to develop a high-frequency X-ray modulation device. One of the most popular types of two-dimensional X-ray imaging systems is the Kirkpatrick-Baez (K-B) piezoelectric deformable mirror. This technology enables the differentiation of individual speckles, ensures speckle homogeneity throughout the imaging exposure, and allows for the deliberate disruption of coherent beam speckles under dynamic mirror surface conditions.

This article presents the design and construction of a testing system specifically tailored for the decoherence of deformable mirrors. It encompasses an in-depth analysis and rigorous testing to explore the interplay between coherence and pivotal parameters, including vibrational frequency and displacement. These investigations are conducted through a combination of meticulous opto-mechanical design and extensive experimental procedures.

II. Deformable mirrors and *ex-situ* measurements

Deformable mirrors

Our design integrates a series of stacked piezoelectric ceramic structures within the piston-type piezoelectric actuators. As depicted in Fig.1(a), these structures consist of 12 piezoelectric ceramic blocks, aligned along their longitudinal axis with a uniform gap of 2 mm separating each pair of blocks. Each ceramic block features an even distribution of 6 pairs of electrodes, with

https://doi.org/10.1017/hpl.2025.7 Published online by Cambridge University Press

each electrode pair having a diameter of 1.5 mm on the bottom surface. Two adjacent pairs of electrodes are connected in parallel, sharing the same voltage potential. Consequently, this configuration results in a total of 36 independent voltage inputs for each mirror. These actuators exert controlled pushes and pulls on the mirror surface, thereby generating high-frequency vibrations, as illustrated in Fig.1(b). The piezoelectric ceramic material used is DM21S, characterized by a Poisson's ratio σ of 0.36, a Curie temperature T_c of 230 ºC, a Young's modulus E of 56 Gpa, a piezoelectric constant d_{33} of 710×10^{-12}C/N, and a frequency constant N_3 of 1500 Hz·m. Each stack of piezoelectric ceramic consists of n = 70 layers, with each layer having a thickness of 42 μm, which means the total electrode height is approximately 2.94 mm and the capacitance is about 50 nf. The displacement $\Delta L = n d_{33} U$ is directly proportional to the applied voltage U, thus allowing the theoretical maximum displacement of the stacked piezoelectric ceramics under no load and at a 50 V voltage to exceed 2 μm. Furthermore, the theoretical maximum resonant frequency of these ceramics can reach approximately 250 kHz.

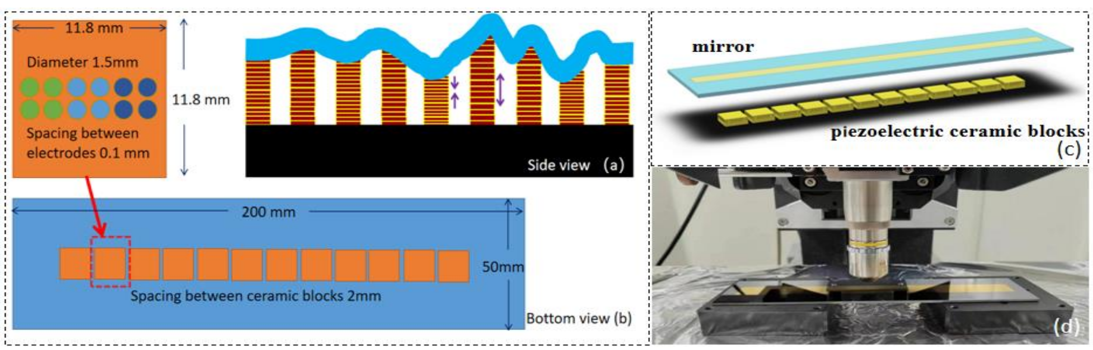

Figure 1 Schematic diagram of modulation of surface shape by stacked piezoelectric piston actuator: (a) demonstration of piston-type piezoelectric actuators from the side view; (b) arrangement of actuator electrodes at the bottom of the mirror;(c) the exploded view of the mirror ;(d) the mirror with the gold film measured by profile.

The dimension of each deformable mirror is 200 mm × 50 mm × 2 mm. As depicted in Fig.1(d), the ZYGO profiler assessed the root mean square roughness of the silicon mirror

https://doi.org/10.1017/hpl.2025.7 Published online by Cambridge University Press

surface and found that it was 0.37 ± 0.07 nm. To ensure a secure bond with the piezoelectric actuators, the mirrors' bottom surfaces were polished as well. An 80 nm layer of gold was deposited on the surface of each mirror to enhance reflectivity. Taking into account the mirror's slender profile, a 40 mm thick stainless steel block was seamlessly integrated into the clamping mechanism's design. Piezoelectric ceramics are adhered to the block surface using glue, creating a unified structure. The block's lower surface features a cone, V-groove, and a flat surface, which are designed to be supported by the base plate, ensuring the high stability of the mirror as depicted in Fig.2(b). This block serves to support the thin mirror and counteract the effects of increased gravitational forces, thus ensuring stability during the high-frequency vibrational processes. The mirror adjustment mechanism is securely mounted to the stainless steel block via the clamping mechanism's base plate. This clamping mechanism has been engineered to achieve submicron precision in both its pushing and bending operations, effectively correcting any minor distortions in the thin mirror that may arise due to clamping stress. Figs.2(a) and (b) present the three-dimensional design drawing of the mirrors and their respective mechanism systems. Fig.2(c) shows the photograph of the piezoelectric ceramics and stainless steel block prior to the mirror's attachment. Furthermore, the manipulator system enables precise adjustments in both position and angle, with capabilities extending into the submicron and submicron radians ranges, ensuring a high degree of accuracy and control.

https://doi.org/10.1017/hpl.2025.7 Published online by Cambridge University Press

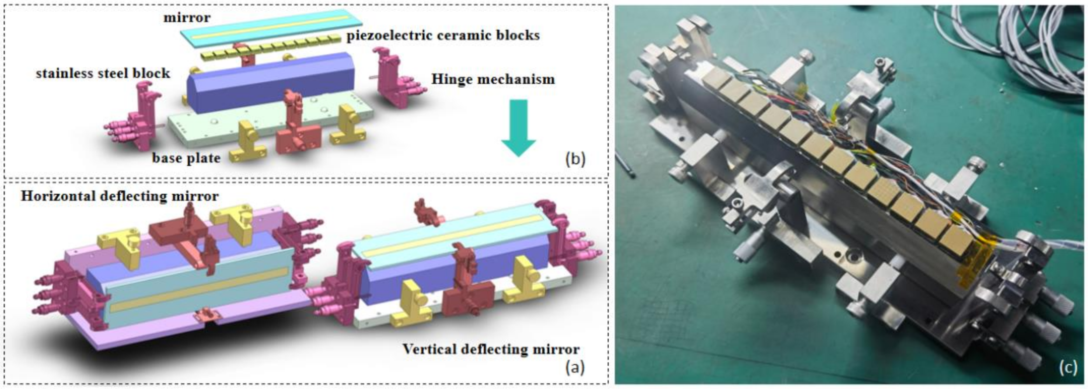

Figure 2 (a)The design drawing of the clamping and adjusting mechanism of the K-B mirror; (b) the 3D exploded view of the vertical deflecting mirror and (c) the photography of the piezoelectric actuators stick on a thick stainless steel block.

High-voltage power supply

The stacked piezoelectric ceramic materials can be actuated by a high-power AC control power supply capable of delivering a maximum voltage of 50 V, allowing for the frequencies up to 100 kHz. The voltage applied to any given actuator follows a sine function and adheres to a specific relationship equation:

$$U = U_{\max} \sin(2\pi ft + \varphi_0), \tag{1}$$

where $U_{\max}$ represents the highest voltage that the power supply can apply, and f denotes the activation frequency, and φ_0 signifies the initial phase of the vibration. To effectively disrupt and modulate the coherence of the beam, the height deviation between adjacent surface shapes must surpass the Rayleigh criterion. This requirement is mathematically expressed through the following inequality:

$$\Delta h > \frac{\lambda}{8\sin\theta}, \tag{2}$$

where λ is the wavelength and θ is the grazing incidence angle of the mirror. Upon the application of a voltage, each actuator is capable of producing a protrusion with a Gaussian

https://doi.org/10.1017/hpl.2025.7 Published online by Cambridge University Press

distribution of height across its original flat surface. The distribution of this protrusion's height can be mathematically expressed as follows:

$$\Delta h = \frac{AU}{\sqrt{\pi / 2}\sigma_a} \exp(-\frac{2x^2}{\sigma_a^2}) , \tag{3}$$

where A is the coefficient, and σ_a is the half width of the piezoelectric response function.

The multi-channel digital high-voltage control power supply is a sophisticated programmable system that comprises three interconnected components: a main control unit, a power transfer module, and a power supply segment. Its logical schematic is depicted in Fig.3. The main control unit is at the heart of the system, featuring an advanced control chip coupled with a suite of peripheral circuits. The main control unit consists of the STM32F407 main control chip from STMicroelectronics, which has a main frequency of 168 MHz, an oscillation circuit, and a reset circuit. The maximum SPI communication speed is 45 Mbit/s. The Ethernet communication chip model is W5500. The main control unit also integrates a user-friendly control panel, a digital-to-analog converter (DAC) for precision control, and a robust network communication interface that ensures seamless connectivity. The DAC control chip uses the DAC81416 chip, which is produced by Texas Instruments and features an integrated internal reference voltage for 16 channels of 16-bit high-voltage output DACs. The power transfer section is engineered for efficiency and reliability, encompassing the DAC for signal conversion, a power conversion subsystem that manages energy flow, an effective heat dissipation mechanism to maintain optimal operating temperatures, and a durable chassis that houses the components. The power supply provides a stable and continuous flow of power to the entire system.The power supply is a direct current (DC) amplified high-voltage amplifier composed of a DAC+ interface and a conversion part.

https://doi.org/10.1017/hpl.2025.7 Published online by Cambridge University Press

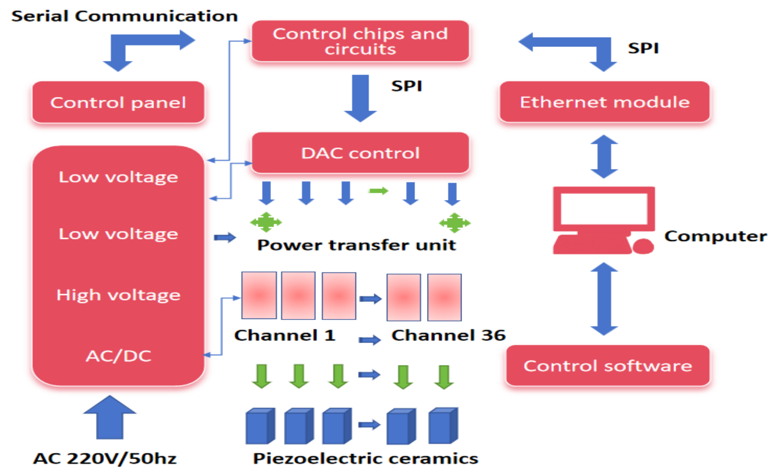

Figure 3 Logic diagram of piezoelectric ceramic control process.

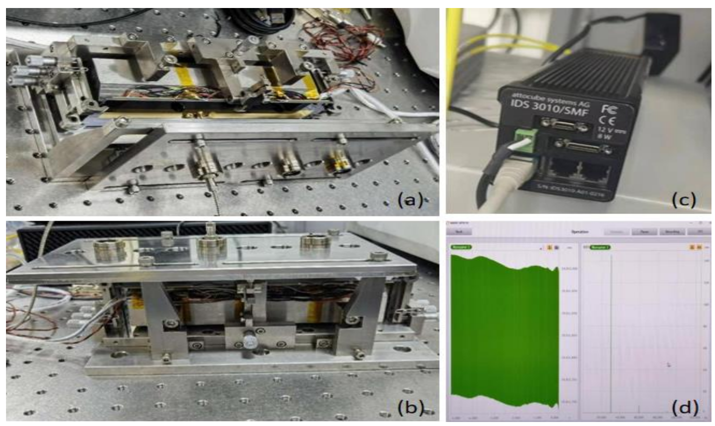

Figure 4 Ex-situ experiments for (a) horizontal deflecting and (b) vertical deflecting mirror by using (c) a laser interferometer with (d) the high-frequency data acquisition software named IDS Feature: wave basic.

Ex-situ measurements

The amplitude and vibrational frequency of the mirror surface, upon the application of voltage to each actuator, were measured using a high-precision laser displacement measuring interferometer (Attocube IDS 3010/SMF, Fig.4(c)). As can be seen in Figs.4(a-b), a stainless steel frame was utilized to hold two mirrors in place during the measurement process. An optical fiber probe, mounted on a movable plate, was positioned over the surface of each mirror to

https://doi.org/10.1017/hpl.2025.7 Published online by Cambridge University Press

facilitate measurements with the sensor resolution of 1 picometer and the fast acquisition rate up to 10 MHz, as depicted in Fig.4(d). Fig.5(a) documents the amplitudes across different electrodes for both mirrors when a voltage of 50 V and a frequency of 30 kHz were applied to each actuator. The average amplitudes for the horizontal and vertical deflecting mirrors were measured to be 141.07 ± 50.44 nm and 166.62 ± 52.27 nm, respectively. Notably, the actuators located at the center and the edges of the mirror demonstrated larger amplitudes. This variation is primarily likely due to the differences in force constraints imposed by the support of the stainless steel block and the clamping. Furthermore, Fig.5(b) captures the amplitudes as a function of varying actuation frequencies, up to 100 kHz, for the 17^{th} actuator of the vertical deflecting mirror. When the driving frequency is 50 kHz, the maximum amplitude can reach 400 nm. This data provides valuable insights into the behavior of the mirror system under different operational conditions. With the Fizeau interferometer, the surface profile of the entire high-speed deformation can be measured. For the average surface shape in the 1 second acquisition time for given actuation frequencies and voltages, the repeatability of less than 3 nm (RMS) was achieved in 10 minutes.

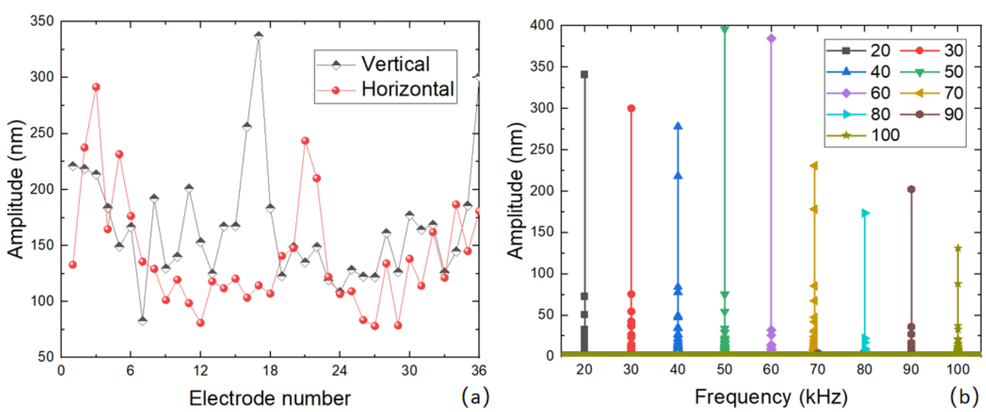

Figure 5 (a) The amplitude of mirror surface for different actuators for two mirrors and (b) the amplitude of 17^{th} actuator versus different frequencies.

https://doi.org/10.1017/hpl.2025.7 Published online by Cambridge University Press

III. Modulation scheme and simulation

Modulation scheme

It is a well-established principle that to effectively deconstruct beam coherence and attain a substantial amplitude, the maximum voltage $U_{\max}$ should be as large as possible. To reduce the phase difference within the divergence angle of the beam, a strategic approach is to assign markedly different initial phases to adjacent actuators. Beyond voltage and initial phase adjustments, varying the frequency at different positions across the mirror surface can further disrupt the correlation of the surface shape under various exposure conditions. Drawing on these premises, our simulation investigated three unique deformation modes to pinpoint the most effective adjustment mechanism for the deformable mirror surface, as illustrated in Fig.6. A pre-set phase was contemplated to address the challenge of implementing swift random phase adjustments in real-time by initiating the phase at a random value. In the case of mode 3, the frequency for every several actuators as a period was altered by a unique coefficient to disrupt the overall phase correlation.

Considering high repetition rate light sources can achieve frequencies up to the MHz range, and given that the mirror surface's deformation vibrations are on the order of tens of kHz, each vibrating surface may experience multiple pulse irradiations during high repetition events. The simulation for a single surface under different pulses can refer to the scenario of non-deformed vibration, and the actual number of collected data points should align with the actual frequency of the deformable mirror surface. For an imaging duration of approximately 1-10 seconds, this equates to 1-100000 deformations. However, the data presented in this article is capable of simulating, at most, 3000 iterations. Consequently, the effects attributed to the deformable mirror may be somewhat underestimated.

https://doi.org/10.1017/hpl.2025.7 Published online by Cambridge University Press

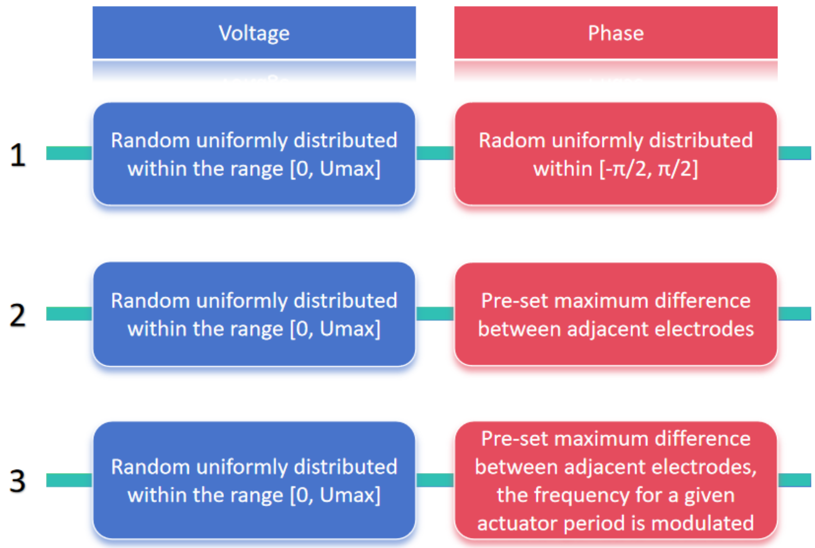

Figure 6 Three distinct deformation modes for actuator modulation.

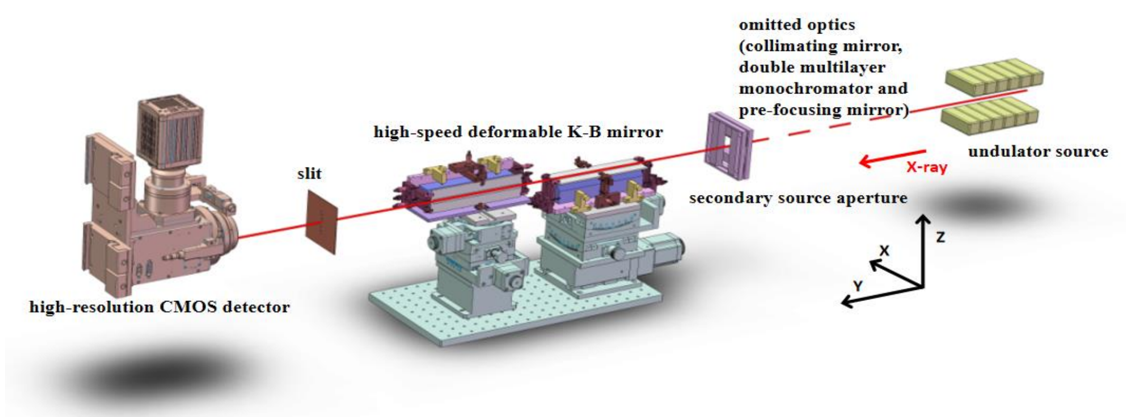

Figure 7 Schematic diagram of the optical path for single-slit diffraction.

Simulation

In this simulation, light source, such as the secondary light source shown in Fig.7, is emulated using a model based on an array of point light sources. Each cluster of pulse beams is arranged in a matrix array configuration on the XZ plane at the exit surface of the secondary source aperture. The two-dimensional normalized beam intensity distribution for these beam clusters adheres to a Gaussian distribution pattern:

https://doi.org/10.1017/hpl.2025.7 Published online by Cambridge University Press

$$I = \exp(-\frac{x^2}{2\sigma_x^2} - \frac{z^2}{2\sigma_z^2}) \tag{4}$$

where $\sigma_{x/z}$ represents the half-width of the beam intensity distribution at the secondary source. The size of each point light source corresponds to the actual physical dimensions. The phase at each position within the array is assigned a random value, uniformly distributed within the range of [-π, π]. For high repetition rate beams, each pulse is considered independent, meaning that the phase distribution array of the source for each pulse is completely different.. The X-ray beams propagate freely along the Y-axis towards the K-B mirror. After two reflections off the K-B mirror, the beams ultimately reach either the slit or the detector. Given that the simulated optical path involves a full coherent or partial coherent beam, the complex amplitudes of the spherical waves emitted from each point light source directly contribute to an amplitude superposition within the specified angular divergence. The intensity distribution at the detection surface is determined by calculating the modulus squared of the superposition of these complex amplitudes. The intensity distribution resulting from the superposition of these point light sources is considered to be an incoherent summation of their respective diffraction intensities. The minimum size of the speckle pattern has a specific relationship: $s_{\min} = 1.22\lambda L / d$,where L is the distance from the mirror to the detector, and d is the spot size. For a speckle pattern, contrast $C = \sigma / \bar{I}$ can be used to estimate the overall clarity of speckle, with lower contrast indicating a disruption of beam coherence, where σ is the RMS intensity fluctuation and $\bar{I}$ is the average intensity.

Throughout the propagation process, there are three distinct steps of free space propagation: the first from the light source to the vertical deflection mirror, the second from the vertical deflection mirror to the horizontal deflection mirror, and the third from the horizontal

https://doi.org/10.1017/hpl.2025.7 Published online by Cambridge University Press

deflection mirror to the detector. For each of these propagation steps, the Huygens-Fresnel diffraction formula is applied to accurately model the behavior of the light waves:

$$\mathrm{U}(P_1)=\frac{1}{\mathrm{j}\lambda}\iint_{\Sigma} U(P_0)\frac{\exp[\mathrm{jk}(r_{01})]}{r_{01}}\cos(\theta_{01})\mathrm{d}s\ . \tag{5}$$

Among them, $U(P_1)$ represents the complex amplitude at observation point P_1, and $U(P_0)$ represents the complex amplitude at point P_0, s is the facet at the diffraction surface Σ, j is an imaginary unit, k is the wave vector of the beam, and r_{01} represents the distance between points P_0 and P_1, θ_{01} represents the angle between the line connecting P_0 and P_1 and the normal at surface P_0.

Single-slit diffraction [23,24] serves as a straightforward method for measuring the coherence of a beam. This process involves the interference and subsequent divergence of beams as they encounter an aperture that is similar in size to the beam's wavelength. The type of diffraction pattern observed—whether Fresnel or Fraunhofer fringes—depends on the slit-to-detector distance when X-ray photons traverse a slit of width a. The coherence of the beam at a specific point can be inferred from the visibility of these fringes. The visibility of the central fringe, in particular, can be determined using the following expression, which relates to the coherent length of the beam:

$$V = V_0 \exp\left(-\frac{a^2}{8l_{tc}^2}\right) = \frac{I_{\max} - I_{\min}}{I_{\max} + I_{\min}} \tag{6}$$

where $I_{\max}$ and $I_{\min}$ are the local maximum and minimum intensities near the center fringe, l_{tc} is the beam transverse coherence length and V_0 is the visibility of the central fringe in the case of point source, given by the [20].

https://doi.org/10.1017/hpl.2025.7 Published online by Cambridge University Press

First simulation aimed to study the effectiveness of deformable mirror scheme. The mirror shape actuated by 36 completely random voltages with different maximum value and the visibility and contrast of the reflective imaging were used to evaluate the beam coherence. Fig.8 illustrates the variations in visibility and contrast of two-dimensional speckle patterns under the influence of different amplitudes of random vibration. When the amplitude of vibration exceeds a peak-to-peak (PV) value of 4 nm, there is a marked disruption in coherence, leading to a notable reduction in both visibility and contrast. The results were in agreement with the Rayleigh criterion.Upon reaching a PV amplitude of 18 nm for the random vibration of the surface, after accumulating 600 samples, the contrast can be diminished to as low as 0.04, while the visibility can be reduced to 0.18.

We conducted a comparison of the local speckle patterns under three distinct operational modes: no mirror vibration, random vibration with random phase, and random vibration with a pre-set phase as described in modulation scheme. This comparison was made after acquiring 1, 5, 100, and 500 exposure samples, respectively. Fig.9 presents a comparative analysis of the contrast curves for several deformable mirror vibration strategies following 500 samples. After long-term exposure, speckle patterns cannot be entirely eliminated in the absence of vibration, and even when the phases of the pulse beams vary, the contrast is at best reduced to 0.33. However, employing a deformable mirror can significantly diminish the contrast of the speckles to below 0.06. It appears that the rate of speckle homogenization increases with the number of random parameters introduced into the system. Mode 1 described in Fig.6 can diminish the contrast to below 0.04 after 500 exposures. Mode 3 was proved to be very effective to reduce contrast compared to mode 2. By increase the voltage, mode 3 can achieve the same effect of mode 1. As can be seen in Fig.10(b), after accumulating 3000 vibration samples, the system with

https://doi.org/10.1017/hpl.2025.7 Published online by Cambridge University Press

random vibration and pre-set phase, along with partial frequency modulation, shows a visibility approaching 0.08 and a contrast that can be lowered to an exceptionally low value of 0.02. The trend in the data suggests that these values can continue to decline.

Fig.10(a) depicts the initial shape of the light spot following 5, 100, and 500 times of homogenization. Under the current modulation mode, while the speckle characteristics undergo significant changes, the position and general shape of the light spot remain essentially unchanged. Upon completion of 500 homogenization cycles, a marked reduction of the speckle contrast is observed, culminating in a light spot that is notably more uniform in appearance

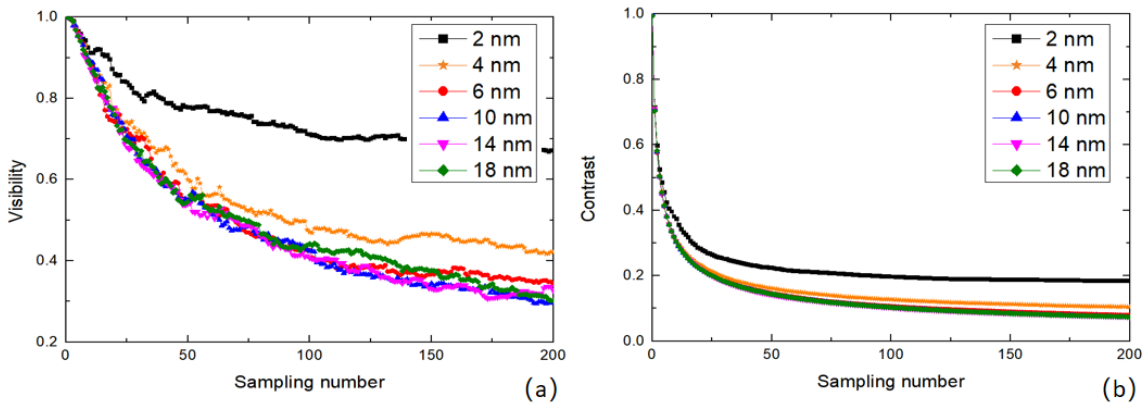

Figure 8 The (a) visibility and (b) contrast of imaging at different PV vibrational amplitudes from 2 nm to 18 nm vary with the increase in the sampling number.

https://doi.org/10.1017/hpl.2025.7 Published online by Cambridge University Press

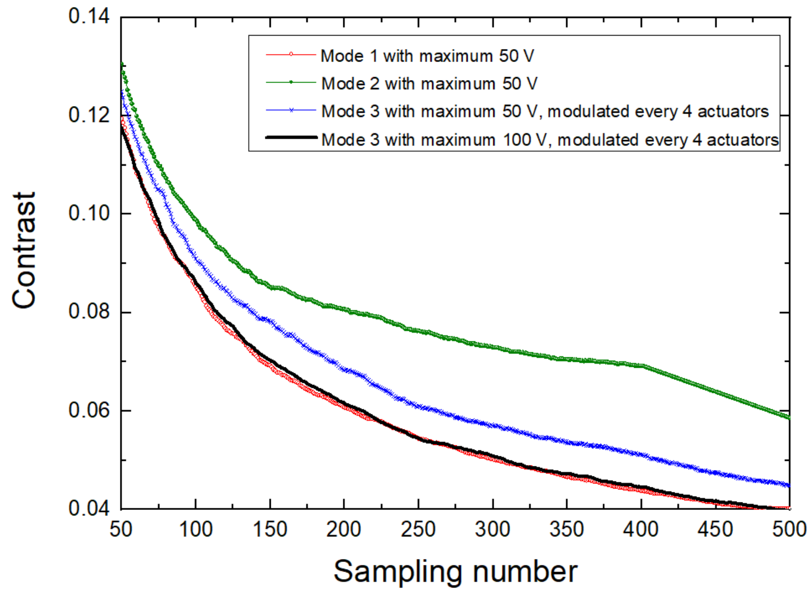

Figure 9 Comparison of the contrasts with different modulation schemes.

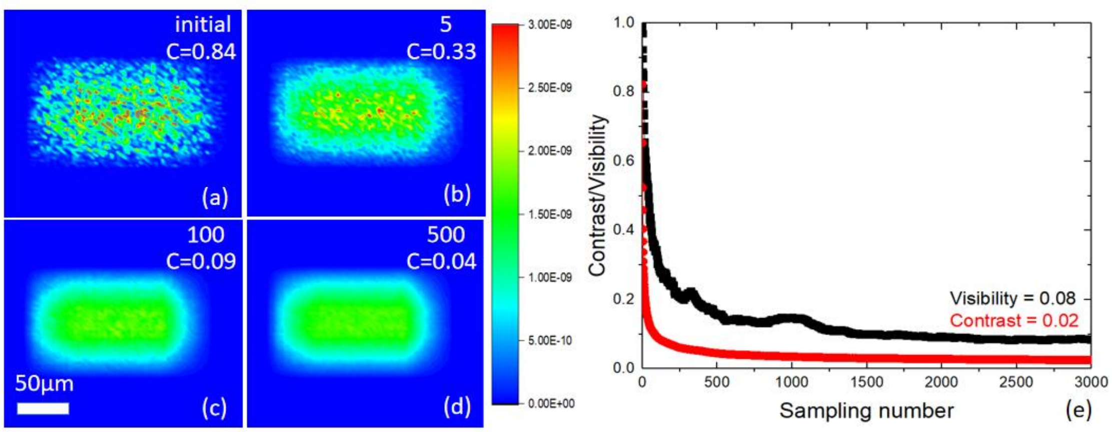

Figure 10 Comparison of the (a) initial light spot and the spot after (b) 5, (c) 100 and (d) 500 times of homogenization and their contrasts;(e) the visibility and contrast as the increase of sampling number.

IV. *In-situ* experiments

The *in-situ* measurement was carried out at the hard X-ray nanoprobe beamline (BL13U) with an operational energy of 10 keV. The comprehensive layout of the beamline is detailed in [25,17].

https://doi.org/10.1017/hpl.2025.7 Published online by Cambridge University Press

Fig.7 displays the schematic diagram for an *in-situ* single-slit diffraction experiment, which is engineered to induce beam decoherence. In the context of the imaging experiment, the slit was removed. The distance spanning from the pre-focusing mirror to the secondary source aperture (SSA) is established at 23 m. The slit opening of SSA was 50 μm (H) × 20 μm (V) to keep a relatively high degree of coherence. The K-B mirror system is situated approximately 67 m downstream from the SSA. The grazing incidence angle for each mirror was 2.1 mrad. A four-bladed slit is positioned 400 mm downstream of the central region of the K-B mirror system. Subsequently, a microscope objective lens system with 50 μm-thickness YAG:Ce scintillator, integrated with a complementary metal-oxide-semiconductor (CMOS) camera, is positioned 1872 mm downstream from the slit. The detector is equipped with a pixel size of 0.65 μm, arrayed in a 2048 × 2048 pixel grid. The exposure time for each image was 10 seconds.The actuation frequency of all channels was 30 kHz.

Figs.11 display the actual image from the *in-situ* test. Under consistent experimental conditions, the diffraction fringes were measured multiple times, yielding curves that are in good agreement with an average deviation of 0.40%. Figs.12 illustrate the application of different maximum random voltages to the mirror, which is actuated by 36 channels. The single-slit diffraction fringe patterns evolve through various phases with an initial setting. The slit width for the single-slit diffraction is set at 85 μm in both horizontal and vertical directions. In this scenario, the theoretical visibility V_0 in Eq.6 is 0.289. As the random maximum voltage applied increased, the significant decrease of the visibility of diffraction fringe can be observed. There are several ripples in the periphery apart from the vicinity of the slit opening. This was caused by the partial oblique incidence of beam due to shape errors.

https://doi.org/10.1017/hpl.2025.7 Published online by Cambridge University Press

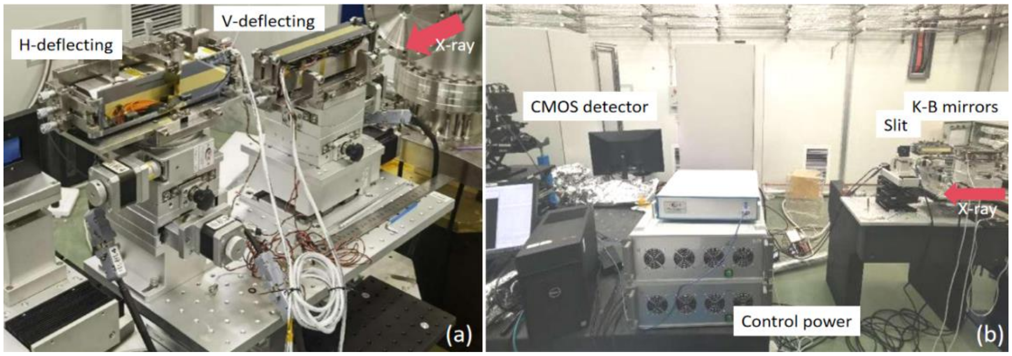

Figure 11 The photos of (a) the K-B system and (b) the overall experimental layout.

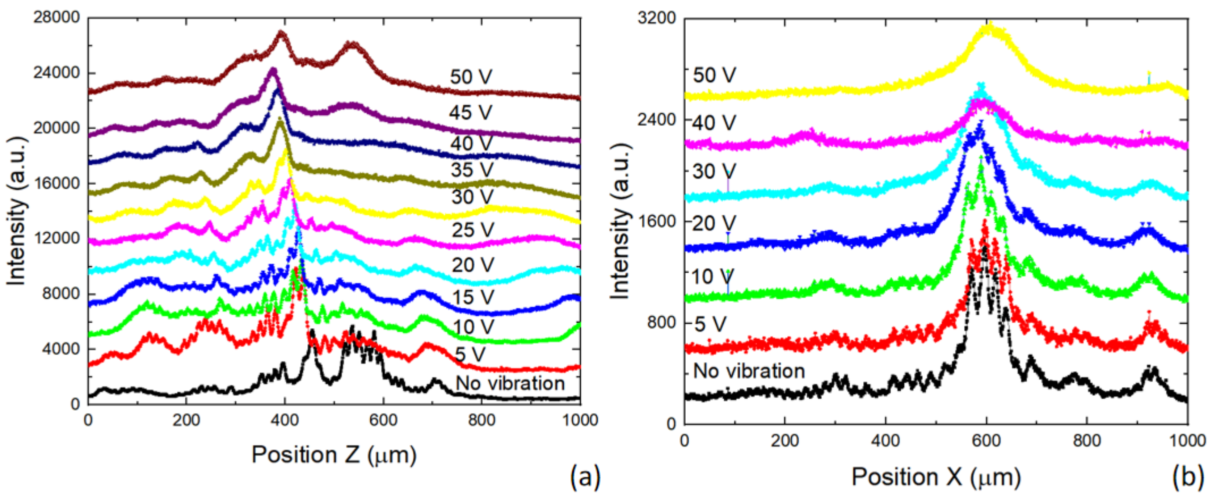

Figure 12 The single-slit diffraction along the (a) vertical and (b) horizontal directions as the increase of the action voltage.

Fig.13 compares the changes in fringe visibility at the central region of the diffraction pattern under different maximum random voltages. The findings indicate that the visibility drops from over 0.20 without vibration to around 0.05 at 20 V. Furthermore, the streaks within the spot are nearly eliminated when the vibration is increased to 50 V, signifying that the coherence has been effectively disrupted. Based on Eq.6, the calculated transverse coherence lengths are found to decrease from 76 μm to 13 μm in the horizontal direction and from 56 μm to 11 μm in the vertical direction. Consequently, the degree of coherence is reduced from over 80% to approximately 13%.

https://doi.org/10.1017/hpl.2025.7 Published online by Cambridge University Press

The CMOS high-resolution imaging system is also capable of directly capturing the reflected beam's spot and subsequently calculating the contrast of the beam speckle, as depicted in Figure 14(a-d). The test results presented in Fig.14(b) demonstrate a significant reduction in imaging contrast with an increase of voltage. Specifically, the contrast is observed to decrease by 0.037 at the maximum voltage of 50V.

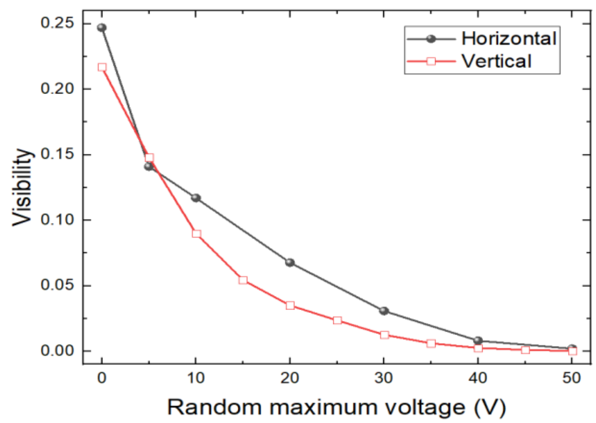

Figure 13 The visibility of the single-slit diffraction as the increase of the random maximum voltage.

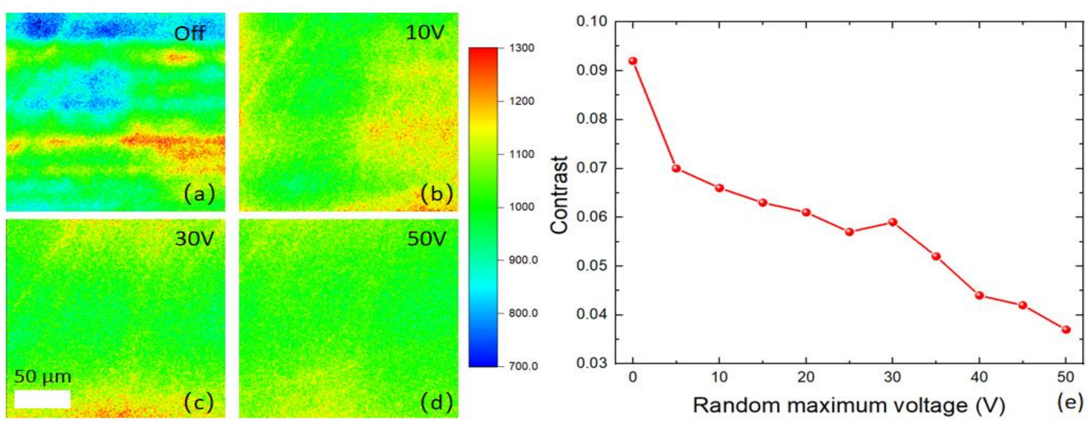

Figure 14 The imaging with the speckles while (a) no voltage applied, maximum (b) 10 V, (c) 30V and (d) 50 V applied; (e) comparison with the contrast of the images as the increase of the maximum voltage.

https://doi.org/10.1017/hpl.2025.7 Published online by Cambridge University Press

V. Conclusions

We have successfully demonstrate a high-speed piezoelectric deformable Kirkpatrick-Baez mirror system that can rapidly change the mirror shape and modulate the X-ray beam uniformity and reduce the coherence. The high-frequency vibration's frequency and amplitude were confirmed using a laser interferometer that recorded data at a 10 MHz acquisition rate. The amplitude of the vibrations exceeded 140 nm, while the frequency reached 100 kHz. At the hard X-ray nanoprobe beamline of the SSRF, an *in-situ* test was conducted. The modulation of the beam's coherence characteristics under high-frequency random vibration was confirmed, and single-slit diffraction and imaging techniques were used to verify the influence of vibration on the visibility of diffraction fringes and the speckle contrast in imaging, respectively. The results demonstrated that the equipment met the requirements of decoherence and could obtain a contrast better than 0.04.

The simulations and experiments prove the effectiveness of X-ray high-speed piezoelectric deformable mirror on beam decoherence and speckle reduction. The maximum vibrational frequency has been raised to 100 kHz, which nearly satisfies the high-speed imaging experiments at the XFELs with high repetition rate. In the future, it may be raised to MHz to meet the experimental requirements at the picosecond level. However, the mirror must be made extremely thin in order to achieve a very high vibrational frequency and amplitude, which causes significant undesirable shape error when the mirror is clamped and supported. These mirror form errors cause distortion or undesired speckle fringes. It is an urgent issue that will eventually need to be resolved. Better mirror modulation strategies must also be suggested in order to fully deconstruct the beam coherence. Another key technological issue is to build a novel piezoelectric actuator structure with a higher resonance frequency and create a power supply that can support a higher activation frequency and voltage, both of which are necessary to fully satisfy the demand of greater repetition rate for specific dynamic experiments.

Acknowledgement

We are grateful for financial supports from National Key Research and Development Program of China (grant No.2023YFA1608604); National Natural Science Foundation of China (grant No. 12175294, 12235011); Natural Science Foundation of Shanghai Municipality (grant No. 21ZR1471500).

References

1. M.Altarelli, “The European X-ray Free-Electron Laser: toward an ultra-bright, high repetition-rate x-ray source”, High Power Laser Sci. Eng. 3:e18.(2015). DOI: https://doi.org/10.1017/hpl.2015.1
2. S.M.Bak, Z.Shadike, R.Lin, X.Q.Yu and X.Q.Yang, “In situ/operando synchrotron-based X-ray techniques for lithium-ion battery research”, NPG Asia Mater. 10, 563–580 (2018). DOI: https://doi.org/10.1038/s41427-018-0056-z
3. F.Pfeiffer, “X-ray ptychography”, Nature Photon. 12, 9-17 (2018). DOI: https://doi.org/10.1038/s41566-017-0072-5
4. W.H.Zhang, J.L.Dresselhaus, H.Fleckenstein, M.Prasciolu, M.Zakharaova, N.Ivanov, C.F.Li, O.Yefanov, T.Li, D.Egorov, I.de.G.Aquino, P.Middendorf, J.Hagemann, S.Shi, S.Bajt and H.N.Chapman, “Fast and efficient hard X-ray projection imaging below 10 nm resolution”, Opt.Express 32(17), 30879-30897 (2024). DOI: https://doi.org/10.1364/oe.532037
5. T.Konstantinova, L.Wiegart, M.Rakitin, A.M.DeGennaro and A.M.Barbour, “Noise reduction in X-ray photon correlation spectroscopy with convolutional neural networks encoder–decoder models”, Sci Rep 11, 14756 (2021). DOI: https://doi.org/10.1038/s41598-021-93747-y
6. S.Matsuyama, S.Yasuda, J.Yamada, H.Okada, Y.Kohmura, M.Yabashi, T.Ishikawa and

K.Yamauchi, “50-nm-resolution full-field X-ray microscope without chromatic aberration using total-reflection imaging mirrors”, Sci. Rep. 7, 46358 (2017). DOI: https://doi.org/10.1038/srep46358

7. R.Cerbino, L.Peverini, M.A.C.Potenza, A.Robert, P.Bosecke and M.Giglio, “X-ray-scattering information obtained from near-field speckle”, Nat. Phys. 4, 238–243 (2008). DOI: https://doi.org/10.1038/nphys837
8. H.T.Lemke, C.Bressler, L.X.Chen, D.M.Fritz, K.J.Gaffney, A.Galler, W.Gawelda, K.Haldrup, R.W.Hartsock, H.Ihee, J.Kim, K.Kim, J.H.Lee, M.M.Nielsen, A.B.Stickrath, W.Zhang, D.Zhu and M.Cammarata, “Femtosecond X-ray Absorption Spectroscopy at a Hard X-ray Free Electron Laser: Application to Spin Crossover Dynamics”, J. Phys. Chem. A 117, 4, 735–740 (2013). DOI: https://doi.org/10.1021/jp312559h
9. S.Kubota and J.W.Goodman, “Very efficient speckle contrast reduction realized by moving diffuser device”, Appl. Opt. 49, 23: 4385-4391 (2010). DOI: https://doi.org/10.1364/AO.49.004385
10. S.Mousavi, E.Plum, J.Shi, I.Nikolay and I.Zheludev, “Coherent control of optical polarization effects in metamaterials”, Sci Rep 5, 8977 (2015). DOI: https://doi.org/10.1038/srep08977
11. N.E.Yu, J.W.Choi, H.Kang, D.K.Ko, S.H.Fu, J.W.Liou, A.H.Kung, H.J.Choi, B.J.Kim, M.Cha and L.H.Peng, “Speckle noise reduction on a laser projection display via a broadband green light source”, Opt. Express 22(3), 3547–3556 (2014). DOI: https://doi.org/10.1364/OE.22.003547
12. T-K-T.Tran, X.Chen, Ø.Svensen and M.H.Akram, “Speckle reduction in laser projection using a dynamic deformable mirror”, Opt. Express 22(9), 11152-11166 (2014). DOI: https://doi.org/10.1364/OE.22.011152
13. H.A.Chen, J.W.Pan, and Z.P, Yang, “Speckle reduction using deformable mirrors with diffusers in a laser pico-projector” Opt.Express 25(15), 18140-18151 (2017). DOI: https://doi.org/10.1364/OE.25.018140
14. M.Booth, “Adaptive optical microscopy: the ongoing quest for a perfect image”, Light Sci. Appl. 3, e165 (2014). DOI: https://doi.org/10.1038/lsa.2014.46
15. Z.Zhou, J.F.Huang, X.Li, X.F.Gao, Z.Y.Chen, Z.F.Jiao, Z.H.Zhang, Q.M.Luo, L.Fu,

"Adaptive optical microscopy via virtual-imaging-assisted wavefront sensing for high-resolution tissue imaging", PhotoniX 3, 13 (2022). DOI: https://doi.org/10.1186/s43074-022-00060-6

16. H.Mimura, S.Handa, T.Kimura, H.Yumoto, D.Yamakawa, H.Yokoyama, S.Matsuyama, K.Inagaki, K.Yamamura, Y.Sano, K.Tamasaku, Y.Nishino, M.Yabashi, T.Ishikawa and K.Yamauchi, "Breaking the 10nm barrier in hard-X-ray focusing", Nat. Physics 6(2), 122-125 (2010). DOI: https://doi.org/10.1038/nphys1457
17. H.Jiang, J.N.Xie, Y.He, Z.S.Jiang, D.X.Liang, H.N.Yu and A.G.Li, "Multilayer Kirkpatrick-Baez focusing mirrors with phase compensation for sub-20 nm focusing at the hard X-ray nanoprobe beamline of SSRF", Opt.Express 32, 8: 13597 (2024). DOI: https://doi.org/10.1364/OE.514734
18. S.G.Alcock, I.Nistea, V.G.Badami, R.Signorato, M.Fusco, L.F.Hu, H.Wang and K.Sawhney, "Fast shaping control of x ray beams using a closed-loop adaptive bimorph deformable mirror", Optica 10(2):172-182 (2023). DOI: https://doi.org/10.1364/opticaopen.21947114
19. N.X.Tian, H.Jiang, J.N.Xie, S.Yan, D.X.Liang and Z.S.Jiang, "An active piezoelectric plane X-ray focusing mirror with linear changed thickness", J.Synchrotron Rad. 31(1):10-16 (2024). DOI: https://doi.org/10.1107/S1600577523009566
20. Y.Y.Kim, L.Gelisio, G.Mercurio, S.Dziarzhytski, M.Beye, L.Bocklage, A.Classen, C.David and O.Y.Gorobtsov, "Ghost imaging at an XUV free-electron laser", Phys.Rev.A, 013820 (2020). DOI: https://doi.org/10.1103/PhysRevA.101.013820
21. S. C. Irvine, K. S. Morgan, Y. Suzuki, K. Uesugi, A. Takeuchi, D. M. Paganin, and K. K. W. Siu, "Assessment of the use of a diffuser in propagation-based x-ray phase contrast imaging," Opt. Express 18, 13478-13491 (2010). DOI: https://doi.org/10.1364/OE.18.013478
22. M.Eddah, H.Markötter,B.Mieller, M.Sintschuk,J.Beckmanna and G.Bruno, "Mitigation of DMM-induced stripe patterns in synchrotron X-ray radiography through dynamic tilting", J.Synchrotron Rad. 31, 1551–1560 (2024). DOI: https://doi.org/10.1107/S1600577524008646
23. V.Kohn, I.Snigirev and A.Snigirev, "Direct measurement of transverse coherence length of

https://doi.org/10.1017/hpl.2025.7 Published online by Cambridge University Press

hard X-rays from interference fringes", Phys.Rev.Lett. 85(13):2745-2748 (2000). DOI: https://doi.org/10.1103/PhysRevLett.85.2745

24. H.Jiang, S.Yan, H.Wang, Y.Zheng, Z.H.Dong and A.G.Li, "An equivalent source to describe realistic synchrotron hard X-rays", Appl.Phys.B 122, 271 (2016). DOI: https://doi.org/10.1007/s00340-016-6547-0
25. Y.He, H.Jiang, D.Liang, Z.S.Jiang, H.N.Yu, H.Wang, C.W.Mao, J.Xie, A.G.Li, "The hard X-ray nanoprobe beamline at the SSRF", Nucl.Sci. Tech. 35:121 (2024). DOI： https://doi.org/10.1007/s41365-024-01485-3

https://doi.org/10.1017/hpl.2025.7 Published online by Cambridge University Press